Flow Turbulence Combust (2007) 79:55–82
DOI 10.1007/s10494-006-9066-y

A Three-Dimensional Hybrid LES-Acoustic Analogy Method for Predicting Open-Cavity Noise

Huanxin Lai · Kai H. Luo

Received: 22 November 2005 / Accepted: 13 November 2006 /
Published online: 28 February 2007

Abstract A three-dimensional (3D) hybrid LES-acoustic analogy method for computational aeroacoustics (CAA) is presented for the prediction of open-cavity noise. The method uses large-eddy simulation (LES) to compute the acoustic source while the Ffowcs Williams-Hawkings (FW-H) acoustic analogy is employed for the prediction of the far-field sound. As a comparison, a two-dimensional (2D) FW-H analogy is also included. The hybrid method has been assessed in an open-cavity flow at a Mach number of 0.85 and a Reynolds number of $Re=1.36\times10^6$, where some experimental data are available for comparison. The study has identified some important technical issues in the application of the FW-H acoustic analogy to cavity noise prediction and CAA in general, including the proper selection of the integration period and the modes of sound sources in the frequency domain. The different nature of 2D and 3D wave propagation is also highlighted, which calls for a matching acoustic solver for each problem. The developed hybrid method has shown promise to be a feasible, accurate and computationally affordable approach for CAA.

Key words Ffowcs Williams-Hawkings analogy · large-eddy simulation · hybrid methods · three-dimensional implementation · cavity acoustics · computational aeroacoustics

Nomenclature

C_S	Constant of the subgrid scale (SGS) models
c_∞	Sound speed at free upstream
D	Cavity depth
E	Constant, 9.8
E_T	Total energy defined by Eq. 6
$F_i, \mathcal{F}_i$	Sound source and its discrete Fourier transform

H. Lai (✉)
Fluid Machinery Group, East China University of Science and Technology, Mail Box 401,
130 Meilong Rd., Shanghai 200237, P.R. China
e-mail: hlai@ecust.edu.cn

H. Lai · K. H. Luo
Energy Technology Research Group, School of Engineering Sciences, University of Southhampton,
Southhampton SO17 1BJ, UK

f	A function that defines the moving surface
$\cancel{f}$	Frequency
G	Free-space Green function, Eqs. 16 and 16a
$H\,(f)$	Heaviside function
$H_0^{(1)}$	Hankel function of the first kind and order zero
$H_0^{(2)}$	Hankel function of the second kind and order zero
i	$\sqrt{-1}$
$I\,(x)$	Imaginary part of a complex number x
k	ω/c_∞
l	Turbulence length scale, Eq. 11
L	Cavity length
M	Mach number
p	Static pressure, Eq. 8
p'	Acoustic pressure
Pr	Prandtl number
Pr_t	SGS Prandtl number
q	Heat flux defined by Eq. 7
Q, $\cancel{Q}$	Sound source and its discrete Fourier transform
Q_-	Criterion defined by Eq. 20
r	Radial
$R\,(x)$	Real part of a complex number x
r_β	Source–observer distance in the translating propagation medium, $\sqrt{(x_1-y_1)^2+\beta^2(x_2-y_2)^2+\beta^2(x_3-y_3)^2}$
$r_{\beta 0}$	Source–observer distance with source placed at coordinate origin, $\sqrt{x_1^2+\beta^2\left(x_2^2+x_3^2\right)}$
Re	Reynolds number
s	Vertical distance from the cavity plate to the integration surface
S	Subgrid term of Eq. 3, calculated by Eq. 9
S_{ij}	Strain rate tensor
$\lvert S\rvert$	Absolute value of the strain rate
t	Time
T	Temperature
T_{ij}, $\cancel{T}_{ij}$	Lighthill's stress and its discrete Fourier transform
u_i	Total velocity, U_i+u_i'
u_i'	Acoustic particle velocity
U_i	Constant velocity of the ambient flow
u_τ	Wall shear velocity
v_i	Velocity component of the moving surface f=0
W	Cavity width
x_i, $\vec{x}$, (x, y, z)	Coordinates in the observer zone
y_i, $\vec{y}$	Coordinates in the source zone
y^+	Distance to the wall, expressed in wall units

Greek Symbols

α	Constant of the SGS models
β	Prandtl-Glauert factor, $\sqrt{1-M^2}$ for M<1
δ_{ij}	Kronecker delta function

δ (*f*)	Dirac delta function
Δ	Filter width on the grid level
Δt	Non-dimensional time interval
ϕ	Operator of the discrete Fourier transform
Φ	Angle in the *x*–*z* meridional plane
γ	Ratio of specific heats
κ	von Karman constant, 0.42
μ	Dynamic molecular viscosity
v_t	Kinematic turbulent viscosity
ν	Kinematic viscosity
ρ	Density
σ_{ij}	Viscous stress defined by Eq. 5
τ_{ij}	SGS stress, Eq. 4
ω	Vorticity or angular frequency of the single-frequency monopole
Ω_{ij}	Asymmetric components of the gradient of the velocity vector

Superscripts

~	Favre-filtered variable
–	Space-filtered variable

Subscripts

c	Pertaining to the Nyquist critical frequency
i, *j*, *k*	Free index of the coordinates
i+1, *i*−1	Pertaining to neighbouring grid points to point *i*
inf	Pertaining to the values of the variables at the freestream
P	Pertaining to the first grid point from a wall
rms	Root-mean-square
Σ	Pertaining to the integration surface Σ

1 Introduction

With the great advancement in both computer power and numerical methods in the most recent two decades, computational aeroacoustics (CAA) has undergone rapid development, and numerically predicting cavity sound generation and propagation has attracted much attention [1–4]. As a prototype problem for fluid dynamics and aeroacoustics, compressible flow over cavities features unsteadiness, flow separation and reattachment, three-dimensionality and strong interactions among shear layer instabilities, turbulence, acoustics and structure. These complex processes present typical difficulties encountered in CAA: (1) the presence of an extremely wide range of flow scales, which makes any single computational method insufficient; (2) the extremely small fraction of sound energy compared with flow energy, meaning that a small error in the flow simulation would lead to a large error in the sound prediction; (3) the treatment of numerical boundaries. In order to overcome these problems, high-order numerical schemes [5, 6] must be used to provide very low numerical dissipation and dispersion, and the computational grids need to be very fine. Rowley et al. [4] used a sixth-order accurate compact scheme and a fourth-order Runge-Kutta method in resolving the acoustic fields of cavities. Gloerfelt et al. [7] also used a fourth-order Runge-Kutta method and a dispersion-relation-preserving (DRP) scheme in their direct numerical simulation (DNS). Although DNS, in principle, is capable of resolving all fluid dynamics and acoustics scales in cavity flow, it has been limited by available computing resources to 2D and low-Reynolds-number cases.

An alternative strategy is to develop hybrid methods which combine flow solvers, such as DNS or large-eddy simulation (LES) for simulating the sound source fields, with methods for computing the far-field sound, such as the extended Kirchoff method [8], acoustic analogies and the linearised Euler equations (LEE). Wang et al. [9] recently reviewed various computational techniques for flow-noise prediction, with particular attention to the hybrid methods for their advantage of scale separation. A high-resolution simulation of the near-flow-field provides details of the sound sources, on the basis of which, the acoustic far-field can be decided. The two-step strategy of hybrid methods provides the flexibility of selecting the most appropriate method at each step for different problems. This makes the hybrid methods very successful in a wide range of aeroacoustics problems, such as jet flows [10–16], mixing layers [17], trailing edges [18], pipe flows [19] and unsteady aerofoil motions [20]. Recently, a hybrid method using 2D DNS and the Ffowcs Williams-Hawkings (FW-H) analogy [21] was applied to study the cavity acoustics [7, 22]. Ashcroft et al. [23] tried to combine the Reynolds-averaged Navier-Stokes (RANS) and the FW-H analogies in their study of the cavity flow. However, the flow solver used in these investigations is either too expensive (using DNS) or too crude (using RANS) for studying cavity acoustics in the engineering context. In the meantime, sound problems in engineering problems are generally 2D, but implementation of the FW-H acoustic analogy in these studies is only 2D. A fully 3D hybrid LES-FW-H acoustic analogy has not been implemented and tested in the context of cavity acoustics.

This paper presents a 3D implementation of the hybrid method using LES for computing the sound source and FW-H integration in the frequency domain for the acoustic field. LES is computationally affordable for computing complex flows in engineering devices, and it resolves energy-containing large scales which are important for sound generation but ignored in RANS. The 3D implementation of the FW-H analogy will be assessed and applied to the open-cavity problem.

2 The Hybrid LES-Acoustic Analogy Method

2.1 LES equations and numerical methods

The non-dimensional filtered governing equations for compressible flow [24] are as follows:

$$\frac{\partial \overline{\rho}}{\partial t}+\frac{\partial}{\partial x_i}\left(\overline{\rho}\widetilde{u}_i\right)=0 \tag{1}$$

$$\frac{\partial(\overline{\rho}\widetilde{u}_i)}{\partial t}+\frac{\partial}{\partial x_j}\left(\overline{\rho}\widetilde{u}_j\widetilde{u}_i\right)=-\frac{\partial \overline{p}}{\partial x_i}+\frac{\partial \widetilde{\sigma}_{ij}}{\partial x_j}+\frac{\partial \tau_{ij}}{\partial x_j}+\frac{\partial}{\partial x_j}\left(\overline{\sigma}_{ij}-\widetilde{\sigma}_{ij}\right) \tag{2}$$

$$\frac{\partial\left(\widetilde{E}_{\mathrm{T}}\right)}{\partial t}+\frac{\partial}{\partial x_j}\left[\left(\widetilde{E}_T+\overline{p}\right)\widetilde{u}_j\right]=\frac{\partial\left(\widetilde{\sigma}_{ij}\widetilde{u}_i\right)}{\partial x_j}-\frac{\partial \widetilde{q}_j}{\partial x_j}+S \tag{3}$$

where the over-bar denotes an ordinary filtered variable, while the tilde denotes a Favre-filtered variable. The non-dimensionalisation was performed with reference to quantities in the free upstream. The reference length is the cavity depth. The subgrid scale (SGS) stress tensor τ_{ij} and other filtered quantities are defined as:

$$\tau_{ij} = -\left(\overline{\rho u_i u_j} - \overline{\rho}\widetilde{u}_i\widetilde{u}_j\right) \tag{4}$$

$$\widetilde{\sigma}_{ij} = \frac{\mu}{Re}\widetilde{S}_{ij} = \frac{\mu}{Re}\left(\frac{\partial\widetilde{u}_i}{\partial x_j} + \frac{\partial\widetilde{u}_j}{\partial x_i} - \frac{2}{3}\delta_{ij}\frac{\partial\widetilde{u}_k}{\partial x_k}\right) \tag{5}$$

$$\widetilde{E}_{\mathrm{T}} = \frac{\overline{p}}{\gamma - 1} + \frac{1}{2}\widetilde{u}_i\widetilde{u}_i \tag{6}$$

$$\widetilde{q}_j = -\frac{\mu}{(\gamma - 1)M^2 PrRe}\frac{\partial\widetilde{T}}{\partial x_j} \tag{7}$$

$$\overline{p} = \frac{\overline{\rho}\widetilde{T}}{\gamma M^2} \tag{8}$$

The viscosity is assumed to follow a power law, and its non-dimensional form is $\mu(T)$=$T^{0.76}$. The SGS term S in the energy equation (Eq. 3) consists of seven parts [24]. In this paper, we adopt a simplified SGS modelling of Larchevêque et al. [25]:

$$S = \frac{\widetilde{u}_i\partial\left(\overline{\rho}\tau_{ij}\right)}{\partial x_j} + \frac{\partial}{\partial x_j}\left(\frac{\overline{\rho}v_t}{(\gamma - 1)PrM^2}\frac{\partial\widetilde{T}}{\partial x_j}\right) \tag{9}$$

The SGS model employed is the Smagorinsky eddy-viscosity model (SM), which calculates the SGS stresses as follows:

$$\tau_{ij} - \frac{1}{3}\tau_{kk}\delta_{ij} = \overline{\rho}v_t S_{ij} \tag{10}$$

where v_t=$l^2|S|$, $S_{ij} = \frac{\partial\widetilde{u}_i}{\partial x_j} + \frac{\partial\widetilde{u}_j}{\partial x_i} - \frac{2}{3}\delta_{ij}\frac{\partial\widetilde{u}_k}{\partial x_k}$,$|S| = \sqrt{0.5S_{ij}S_{ij}}$, and τ_{kk} is modelled as $\tau_{kk} = -4\overline{\rho}l^2|S|^2$ according to Vreman [24]. Because in the SM model, τ_{ij} is not automatically diminishingly small as the wall is approached, the length scale l is corrected by the Van Driest damping function:

$$l = C_{\mathrm{S}}\Delta \cdot \left(1 - \exp\left[\left(-y^+/25\right)^3\right]\right)^{0.5} \tag{11}$$

where $y^+ = yu_\tau/v$ is the normalised distance to the wall, C_{S} is the Smagorinsky constant and is set to 0.17. The friction speed u_τ is determined by matching the two-layer wall function:

$$u_{\mathrm{P}}^+ = \begin{cases} y_{\mathrm{P}}^+ & \text{if } y_{\mathrm{P}}^+ \leq 11.13 \\ \kappa^{-1}\ln\left(Ey_{\mathrm{P}}^+\right) & \text{if } y_{\mathrm{P}}^+ > 11.13 \end{cases} \tag{12}$$

where κ=0.42 is the von Karman constant, E=9.8, $u_{\mathrm{P}}^+ = u_{\mathrm{P}}/u_\tau$,$y_{\mathrm{P}}^+ = y_{\mathrm{P}}u_\tau/v$,$u_{\mathrm{P}}$ is the resolved velocity tangential to the wall at the wall-nearest point and y_{P} is the distance from this point to the wall.

The numerical methods for LES in the present study are based on the full compressible Navier-Stokes equations. The code used was previously designed for simulating shock/ boundary-layer interaction (SBLI) [26–28]. An entropy-splitting approach is employed, which splits the inviscid flux to stabilise the solution. Experience shows that such a splitting procedure improves the non-linear stability and minimises the numerical dissipation. Compatible spatial difference operators for interior points and boundary nodes are used. For interior points, a five-point fourth-order central scheme is employed. The boundary points are treated using a stable high-order method based on the summation by parts (SBP) [29]. The overall spatial accuracy is fourth-order. For temporal discretisation, a third-order explicit Runge-Kutta algorithm is employed.

The code uses multi-block meshes and can handle complex geometries. It is parallelised using the MPI algorithm and is optimised for massively parallel computers.

2.2 Acoustic analogy

Compared with other methods for computing the acoustic far-field, acoustic analogies are more versatile and economical. There are two other approaches, Kirchhoff integration and LEE. LEE needs to solve a group of linearised equations on a computational mesh, and the computational cost depends on the locations of the chosen observation points. Contrary to this, Kirchhoff integration and acoustic analogies only solve a scalar equation, and the computational cost is independent of the observation locations. The Kirchhoff method is based on an inhomogeneous wave equation, which is derived by assuming linear wave propagation. In order to reconstruct the wave behaviour, acoustic pressure p' and its time and normal derivatives on the integration surface are required, and the integration surface must be placed in the linear acoustic zone. These requirements restrict the application of the Kirchhoff integration. On the other hand, acoustic analogies pioneered by Lighthill [30] are based on an exact linear wave equation for the density. All non-linear effects are accounted for by the Lighthill stress tensor, which acts as the sound source. Curle [31] extended the Lighthill analogy to include the effects of solid boundaries. Ffows Williams and Hawkings [21] generalised the Curle solution to incorporate the arbitrary motion of aerodynamic surfaces and derived the FW-H equation, which is the most general form of the acoustic analogy. The FW-H equation can be solved in differential or integral forms, and the solution procedure can be in the spatial/temporal, wave-number/temporal or spatial/frequency domains. In this paper, we integrate the FW-H equation numerically in the spatial/frequency domain. In summary, the selection of the FW-H acoustic analogy is based on the following considerations:

(a) Among the methodologies for predicting sound in the far-field, an acoustic analogy is computationally cheaper than the LEE method.
(b) The cavity problem has solid boundaries, so Lighthill's analogy is not suitable. Both the Curle integration [31] and FW-H analogy are applicable to a bounded domain, but the FW-H analogy can handle surfaces in motion, and the surface can be permeable, allowing mass, momentum and energy to pass through it.
(c) Compared with the Kirchhoff method, the FW-H equation has a greater degree of flexibility in positioning the integration surface.
(d) The FW-H analogy equation can be in differential and integral forms. When the integral form is used, the solution can be obtained by convoluting the wave equation with the free-space Green function. The convolution changes the dependent spatial coordinates from the observer's domain into the source zone. Therefore, the observer's domain no longer needs to be a continuous space, but can consist of only a few selected discrete points. This provides great flexibility for studying acoustic signals in specially chosen places, with greatly reduced computational cost.
(e) The integration in the frequency domain can avoid the evaluation of the retarded time.

(f) When the integral surface is placed in the zone where the Lighthill's stresses can be neglected, the volume integration can be omitted and, therefore, the computational cost can be further reduced.

Gloerfelt et al. [7] and Lockard [32] have successfully implemented the FW-H analogy in the spatial/frequency domain in 2D form for sound propagation in a uniform background flow. Here, we present a 3D form. Consider the following differential form of the FW-H equation in a uniform background flow:

$$\left(\frac{\partial^2}{\partial t^2}+U_iU_j\frac{\partial^2}{\partial x_i\partial x_j}+2U_i\frac{\partial^2}{\partial x_i\partial t}-c_\infty^2\frac{\partial^2}{\partial x_i\partial x_i}\right)[H(f)\rho']$$
$$=\frac{\partial^2}{\partial x_i\partial x_j}\left[T_{ij}H(f)\right]+\frac{\partial}{\partial x_i}[F_i\delta(f)]+\frac{\partial}{\partial t}[Q\delta(f)] \tag{13}$$

where U_i is the uniform background flow velocity, $(t,\ x_i)$ are the temporal and spatial coordinates in the observer flow domain and c is the speed of sound, while the subscript ∞ denotes a variable pertaining to the incoming freestream conditions. Function $f(x)$=0 defines an integration surface Σ. f<0 indicates the sound source region and $f>0$ the acoustic field. Without the loss of generality, it is assumed that $|\nabla f|$=1 on $f=0$. $H(f)$ and $\delta(f)$ are, respectively, the Heaviside function and the Dirac delta function:

$$H(f)=\begin{cases}0 & \text{in } \Sigma\\ 1 & \text{elsewhere}\end{cases},\qquad \delta(f)=\frac{\mathrm{d}}{\mathrm{df}}[H(f)]$$

The terms in the quadrupole, dipole and monopole sources in Eq. 13 are defined as:

$$\begin{aligned}T_{ij}&=\rho(u_i-U_i)\left(u_j-U_j\right)+\left(p-c_\infty^2\rho\right)\delta_{ij}-\widetilde{\sigma}_{ij};\\ F_i&=-\left[\rho(u_i-2U_i)u_j+p\delta_{ij}+\rho_\infty U_iU_j-\widetilde{\sigma}_{ij}\right]\frac{\partial f}{\partial x_j};\\ Q&=(\rho u_i-\rho_\infty U_i)\tfrac{\partial f}{\partial x_j},\end{aligned}$$

where the viscous stress $\widetilde{\sigma}_{ij}$ is generally negligible. Applying the Fourier transform:

$$\phi(\vec{x},\omega)=\int_{-\infty}^{\infty}\phi(\vec{x},t)e^{i\omega t}dt\ , \tag{14}$$

to Eq. 13 and convoluting with the free-space Green function, we have the integral form of the FW-H analogy in the frequency domain:

$$\begin{aligned}p'(\vec{x},\omega)H(f)=&\int_{f=0}F_i(\vec{y},\omega)\frac{\partial G(\vec{x}|\vec{y},\omega)}{\partial y_i}d\Sigma+\int_{f=0}i\omega Q(\vec{y},\omega)G(\vec{x}|\vec{y},\omega)d\Sigma\\ &-\int_{f>0}T_{ij}(\vec{y},\omega)\frac{\partial^2G(\vec{x}|\vec{y},\omega)}{\partial y_i\partial y_j}d\vec{y}\end{aligned}, \tag{15}$$

where F_i, Q and T_{ij} are the Fourier transforms of F_i, Q and T_{ij}, respectively, $M_i=U_i/c_\infty$ and $k=\omega/c_\infty$. The 3D free-space Green function is as follows [33]:

$$G(\overrightarrow{x}|\overrightarrow{y},\ \omega)=-\frac{\exp\left(i\frac{k}{\beta^2}\left[r_\beta-M_\infty(x_1-y_1)\right]\right)}{4\pi r_\beta} \tag{16}$$

where $\beta = \sqrt{1-M^2}$ $(M<1)$,$r_\beta = \sqrt{(x_1-y_1)^2+\beta^2(x_2-y_2)^2+\beta^2(x_3-y_3)^2}$,$\vec{x}$ is the observer position and $\vec{y}$ denotes a source point. For a 2D case, the Green function is [33]:

$$G(\vec{x}|\vec{y},\,\omega) = \frac{i}{4\beta} e^{-iMk(x_1-y_1)/\beta^2} H_0^{(1)}\left(\beta^{-2} k r_\beta\right) \tag{16a}$$

where $H_0^{(1)}$ is the Hankel function of the first kind and order zero. The source–observer distance becomes $r_\beta = \sqrt{(x_1-y_1)^2+\beta^2(x_2-y_2)^2}$ for the 2D cases.

In Eq. 15, the position and the shape of the integration surface $f=0$ are not specifically fixed. This provides flexibility for placing the integral surface. If the quadrupole sources are enclosed in the integral surface, the third term on the right hand of Eq. 15 can be omitted.

2.3 Solution procedure

During the LES, a time series of F_i and Q on the integration surface $f=0$ are recorded and transformed into the frequency domain, using discrete Fourier transformation (DFT) to obtain $\mathcal{F}_i$ and $\mathcal{Q}$ The sound pressure in the frequency domain is then calculated using Eq. 15. Finally, an inverse discrete DFT is carried out to obtain the instantaneous sound pressure at the observer position $\vec{x}$.

In 2D near-flow-field computations, the integral surface becomes a curve, along which, F_i and Q will be recorded and the integration will be carried out using the 2D Green function (Eq. 16a).

In the current study, the LES for generating the near-field data is 3D, so the integration surface is selected to be a plane above the cavity and parallel to the cavity plate. The corresponding Green function is Eq. 16. For the convenience of description in the later sections, we call this combination the 3D FW-H.

As a comparison, sound sources along the intersection line between the cavity geometrical central plane and the 3D integration surface are also extracted from the LES. The 2D Green function (Eq. 16a) is employed to predict the sound radiation in the cavity geometrical central plane. This computation is termed the 2D FW-H for the convenience of discussion.

3 Results

3.1 Single-frequency monopole—validation of the analogy

Before applying the 3D and 2D FW-H formulations to a cavity, we first tested the implementations using the sound propagation from a single-frequency monopole source which has an analytical solution.

Consider a single-frequency monopole source located at the origin in a uniform flow in the $+x_1$ direction. The complex potential is constructed by adding harmonic temporal variation to the Green function. Dowling and Ffowcs Williams [34] gave the complex potential of the 2D case. They used the Hankel function of the second kind and order zero, $H_0^{(2)}$, in the 2D Green function because their definition of Fourier transform is different to our Eq. 14. Considering the radiation condition [33], the Hankel function of the first kind and order zero $H_0^{(1)}$ should be used here. The complex potential of the 2D case becomes:

$$\phi(x_1,\,x_2,\,t) = A\frac{i}{4\beta} e^{-i\left(\omega t + Mkx_1/\beta^2\right)} H_0^{(1)}\left(\frac{k}{\beta^2}\sqrt{x_1^2+\beta^2 x_2^2}\right) \tag{17}$$

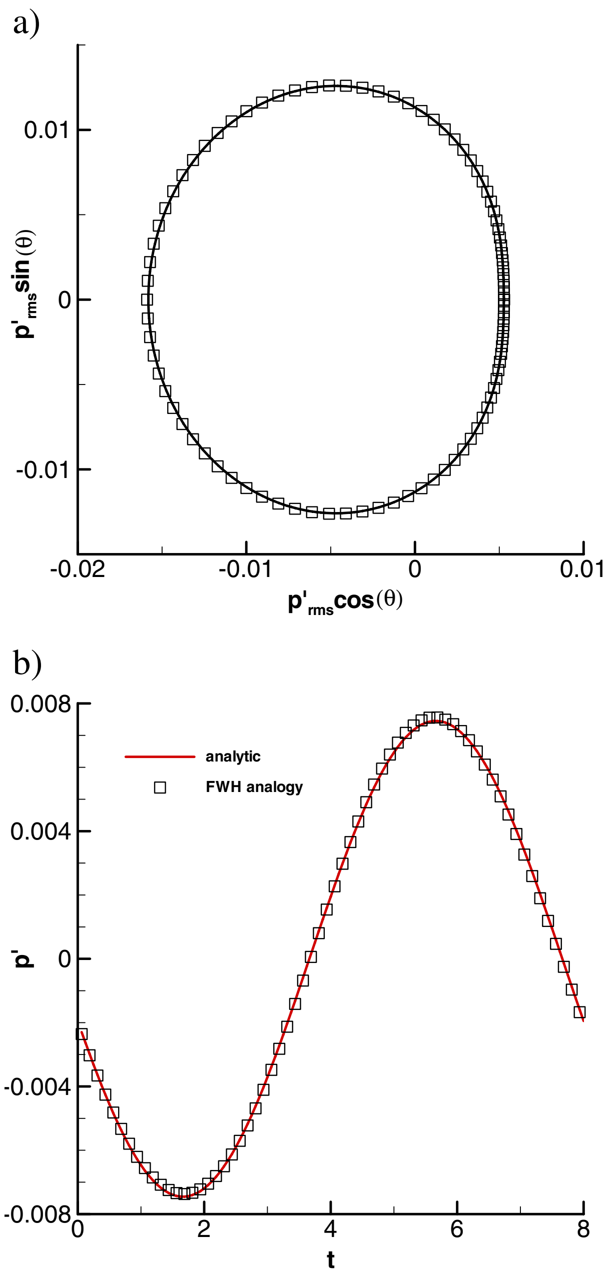

Fig. 1 a, b Comparison of analytical and acoustic analogy prediction of sound from a 2D single-frequency monopole. **a** Directivity at r=500. **b** Time history of sound pressure at (x, y)=(500, 0). *Solid line*: analytical solution, *squares*: FW-H analogy

Similarly, for the 3D case, the complex potential for the monopole is:

$$\phi(x_1,\ x_2,\ x_3,\ t) = Ae^{-i\omega t} \cdot \frac{-\exp\left(i\frac{k}{\beta^2}\left[r_{\beta 0} - Mx_1\right]\right)}{4\pi r_{\beta 0}} \tag{17a}$$

Fig. 2a, b Comparison of analytical and acoustic analogy prediction of sound from a 2D single-frequency monopole. **a** Directivity at *r*=500. **b** Time history of sound pressure at (*x*, *y*, *z*)=(500, 0, 0). *Solid line*: analytic solution, *squares*: FW-H analogy

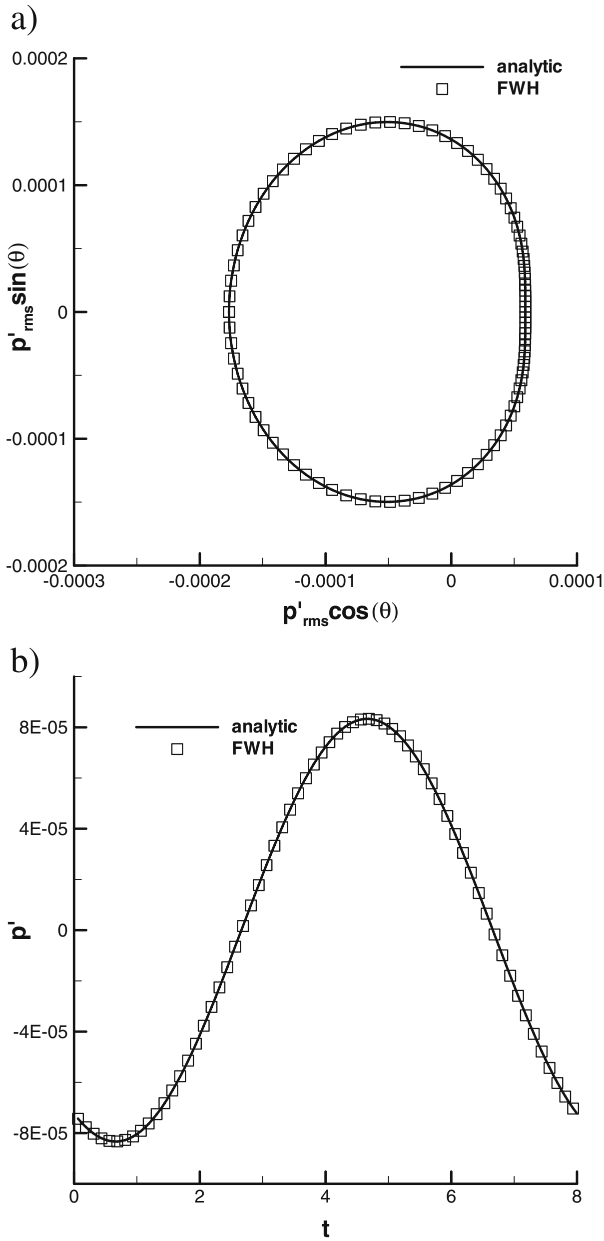

where $r_{\beta 0}=\sqrt{x_1^2+\beta^2\left(x_2^2+x_3^2\right)}$. Quantities needed in the FW-H equation are obtained from the real parts of the following equations:

$$p'=-\rho_\infty\left(\frac{\partial\phi}{\partial t}+U_\infty\frac{\partial\phi}{\partial x_1}\right),\ u_i^{'}=\frac{\partial\phi}{\partial x_i},\ \rho'=\frac{p'}{c_\infty^2}. \tag{18}$$

F_i and Q are evaluated from the flow variables over one period of $\Delta t=\frac{2\pi}{\omega}$ on the integration surface placed at $r=\sqrt{x_1^2+x_2^2}=3$ (cylinder) and $r=\sqrt{x_1^2+x_2^2+x_3^2}=3$

(sphere), for both 2D and 3D cases, respectively. The values for the variables are $M = U_\infty / c_\infty = 0.5$,$\omega$=$\pi$/4 and A=1. The sound pressure at r=500 is calculated by the FW-H equation combined with Eq. 18. Figure 1 compares the analytic solution and the FW-H prediction of the directivity and the time history of the instantaneous sound pressure for the 2D case, while Fig. 2 shows the results of the 3D case. These results demonstrate that the FW-H analogy implemented in both 2D and 3D forms in this study has perfect agreement with the corresponding analytic solutions.

3.2 LES for a 3D cavity

The 3D cavity configuration studied has a length-to-depth ratio of L/D=5 and a width-to-depth ratio of W/D=1. The inflow Mach number is M=0.85, while the Reynolds number is Re=1.36×10^6. This configuration is the high-Reynolds subsonic cavity case extensively measured by the Defence Science and Technology Laboratory (DSTL), UK. Experimental data of unsteady pressure distribution at a series of pressure sensors installed on the cavity walls are provided [35]. The LES simulations carried out in this study correspond to the experimental conditions of Case M219.

An extensive analysis on the flow fields of the cavity has been provided by Larchevêque et al. [36]. The present paper will, therefore, focus on the LES results as the sound sources for the FW-H acoustic analogy, while the flow features are discussed only briefly.

The computational domain shown in Fig. 3 for the current cavity simulation consists of two blocks, BL1 and BL2. BL1 occupies the cavity volume and BL2 consists of the computational domain above the cavity. At the inflow boundary, the mean velocity is specified using a 1/7th power law. The density and temperature are specified according to the Crocoo-Busemann temperature–velocity relation. A small disturbance with the total magnitude of up to 4% of the mean streamwise velocity is added at the inflow boundary. Non-reflecting boundary conditions [37] are applied at the inflow, top and outflow boundaries. On solid walls, a no-slip condition is used for velocity components and an isothermal wall condition is prescribed, with the temperature being equal to the stagnant temperature of the free stream. Meanwhile, the outgoing characteristics are explicitly calculated and are allowed to move out of the computational domain. Sandham et al.'s [26] LES of transonic turbulent flow over a bump using the SBLI code reveals that this boundary treatment can effectively eliminate wave reflections at the boundaries. Periodical conditions are applied in the z direction above the cavity.

Both the upstream and downstream boundaries are located at 4D from the leading and trailing edges of the cavity, respectively, and the upper horizontal boundary is set at H=7D so that the computational domain includes a portion of the acoustic field. For the spanwise direction, two widths for computational domain are tested: W_2=2W and W_2=5W.

For the W_2=2W situation, a total of 5 million grid points distributed in the two blocks in the x–y–z directions are 151×61×61 (BL1) and 301×121×121 (BL2), respectively. The mesh is stretched in the wall-normal direction at a rate of 5% and has nine points located in the viscous sublayer $y^+\leq$11.13, with the first node at y^+=1.26, expressed in non-dimensional wall units and estimated with the inflow quantities. The grid distribution is shown in Fig. 3. For the W_2=5W case, the grids in the overlapping zone with the W_2=2W case are the same. Because of the bigger spanwise length, the number of grid points in the z direction in BL2 becomes 221 and the total number of grid points for the whole computational domain becomes 8.6 million. It should be noted that, in Larchevêque et al.'s LES [36] for this cavity, a fine mesh of 6 million grid points were used. Their computational domain was bigger than our W_2=2W case so that their grid resolution was comparable to the present LES

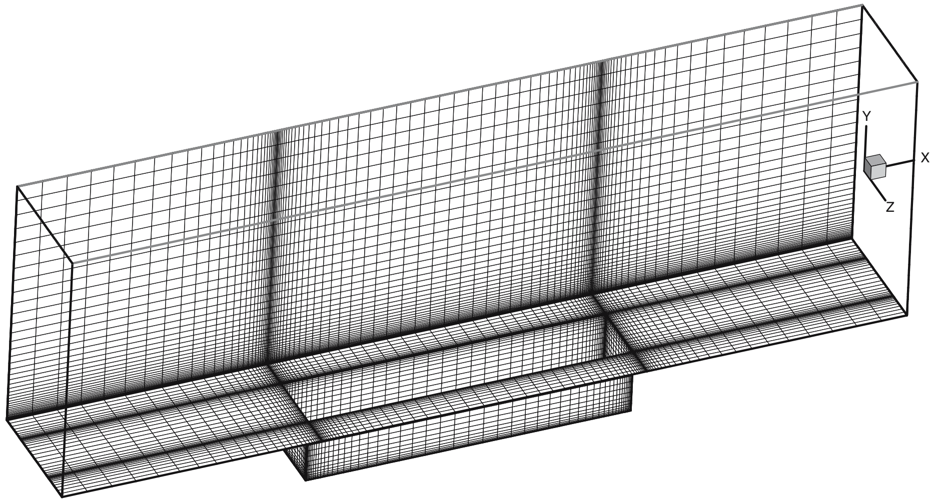

Fig. 3 The multi-block computational domain and grid for LES

case. Meanwhile, Larchevêque et al.'s LES [36] uses second-order schemes for both temporal and spatial discretisation, whereas the present LES has fourth-order and third-order schemes for spatial and temporal discretisation, respectively. Therefore, the overall numerical accuracy of the LES in this study should be comparable to or even slightly higher than that in [36].

The LES simulations were conducted with 64 processors on the UK's HPCx service. The CFL number is set to be 1.0, which corresponds to a non-dimensional time step of about 2.5×10^{-4}. Figure 4 shows a comparison of the non-dimensional sound pressure histories at a monitored point, defined as:

$$p' = p - p_{\mathrm{inf}} \tag{19}$$

at the geometrical centre of the cavity mouth. For the two cases with different spanwise computational domains, the instantaneous pressure traces are quite similar up to a non-dimensional time of about 20, but they become different at later times, though the

Fig. 4 Comparison of pressure histories at the geometrical centre of cavity mouth obtained by LES using a small and a large spanwise computational domain

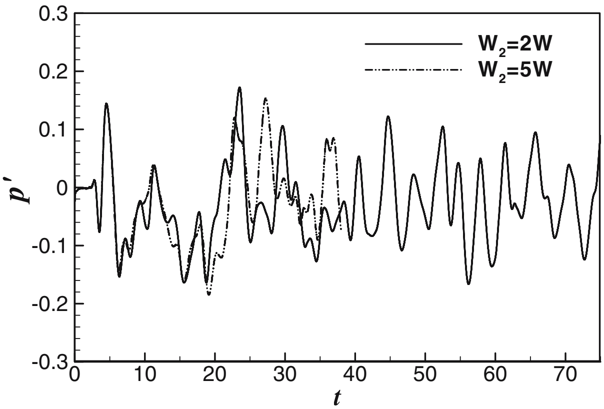

amplitudes of pressure fluctuations for the two simulations remain quite similar. Figure 5 compares the distributions of the averaged and the root-mean-square values of the sound pressure, p'_{av} and p'_{mean}, respectively, along the longitudinal centre line of the cavity wall. The mean values are taken during the interval $0 \leq t \leq 38$. Figure 5 shows that the statistical quantities are very close for the two simulations, despite the differences in the instantaneous oscillation profiles shown in Fig. 4. In the sense of LES, the comparisons in Figs. 4 and 5 indicate that the spanwise computational domain size for the case with $W_2 = 2W$ is large enough, so that, in all subsequent simulations, the narrower spanwise domain size is used in order to reduce the computational cost.

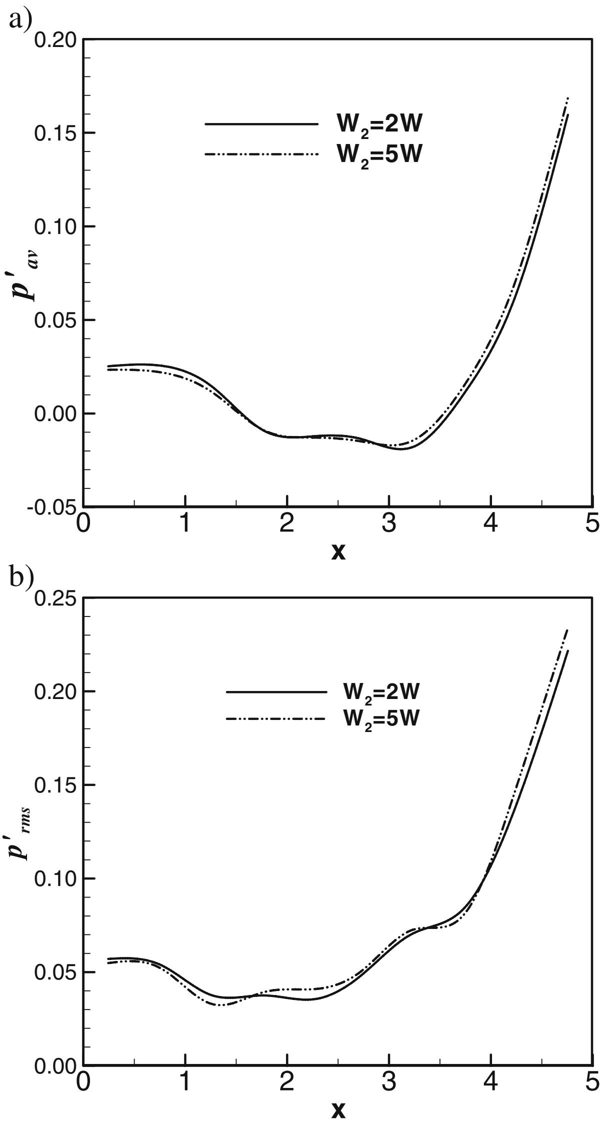

Fig. 5 a, b Comparison of the distributions of the mean sound pressure along the centre line of a cavity floor, obtained by LES using a small and a large spanwise computational domain. **a** Averaged values p'_{av} **b** Root-mean-square values p'_{rms}

The LES for W_2=2W is carried out until t=120. Figure 6 shows the 3D views of the Q_- criterion [38] at three instants during a period Δt_2 corresponding to the second Rossiter mode. The vortex structures are represented by the iso-surface of the Q_- criterion defined as:

$$Q_- = \frac{1}{2}\left(\Omega_{ij}\Omega_{ij} - S_{ij}S_{ij}\right) = -\frac{1}{2}\frac{\partial u_i}{\partial x_j}\frac{\partial u_j}{\partial x_i} > 0 \tag{20}$$

where Ω_{ij} is the asymmetric component of the gradient of velocity vector. So, the Q_- criterion is the second invariant of the velocity gradient. The region enclosed by an iso-surface of a positive Q_- value defines a vortex core. Shown in Fig. 6 are the vortical structures deduced using the iso-surface Q_-=20$(U_{\text{in}}/L)^2$ as in [25]. Quite complex and unsteady vortex structures are featured. Large spanwise vortices are generated periodically near the cavity leading edge, due to the Kelvin-Helmholtz instabilities. These vortices are spanwise rollers extending to the two side walls at the beginning, but quickly become bent in the spanwise direction, so that longitudinal structures start to appear at the roller's two ends. The zone where spanwise vortical structures dominate is much shorter than seen typically in 2D simulations, indicating the early transition to turbulence. Shortly afterwards, the large vortices break up into smaller vortices, which are irregular and highly 3D. The vortical structures are especially complex near the cavity rear wall, due to flow impingement and recirculation. The impingement of flow structures causes a pressure wave travelling upstream, which will interact with the shear layer at the cavity leading edge, trigger further instabilities and complete the acoustic feedback. In the region downstream of the cavity trailing edge, flow separation and reversal occur, followed by streamwise streaks typically found in boundary layers.

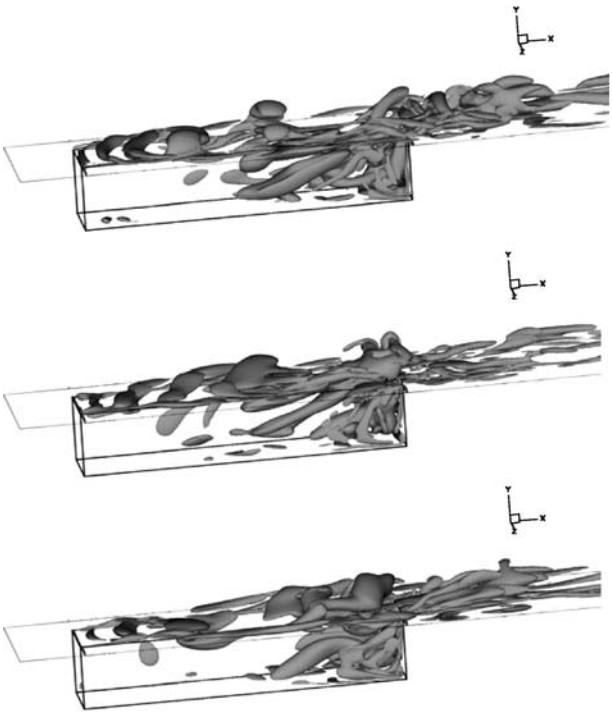

Fig. 6 Three-dimensional vortical structures defined by the Q_- criterion at three instants during a period corresponding to the second Rossiter mode

Figure 7 shows the spectrum of the dimensional pressure against the Strouhal number $St_D = f \cdot D / U_{inf}$ at a monitored point on the cavity floor. For LES results, the spectrum is generated using the instantaneous pressure in the range $62 \leq t \leq 120$, which is a period of non-dimensional time of 58 units and is equal to the sampling time for 128 experimental data. For experimental results, the spectrum shown in Fig. 7 is produced using an ensemble average. The experimental data are divided into 160 window sections, with each section having 128 samples. Data in each section undergo a fast Fourier transformation (FFT). The final spectrum is an ensemble average of the 160 spectra. Figure 7 shows that the LES has well reproduced the frequencies of the first three Rossiter modes n=1 to n=3. However, there is a noticeable difference between the predicted and experimental values of the amplitude for n=3. This is possibly due to the fact that the experimental spectrum is an ensemble average, while the spectrum from LES uses only one sample of data.

Figure 8 compares the sound pressure level (SPL) at a series of monitoring points on the cavity floor along the line z/D=0.625. The SPL is defined as:

$$\mathrm{SPL(dB)} = 20 \log_{10} \left(p'_{\mathrm{rms}} \Big/ 2 \times 10^{-5}\ \mathrm{Pa} \right) \tag{21}$$

The LES result agrees reasonably well with the experimental data, especially in qualitative terms. The main quantitative discrepancies are in the wake zone behind the leading edge of the cavity and in the corner between the rear wall and the cavity floor, where there is a large flow recalculation zone. In these regions, the flow is of relatively low Reynolds numbers and the Smagorinsky model may not be reliable. Bogey and Bailly [39] and Gloerfelt [40] observed that the effective Reynolds number was reduced by using an eddy-viscosity model. As a result, the predicted large vortical structures, which are energy-containing and control the low-frequency tones of the cavity sound, are enhanced by using the Smagorinsky model. This may explain the over-prediction of the SPL in these zones.

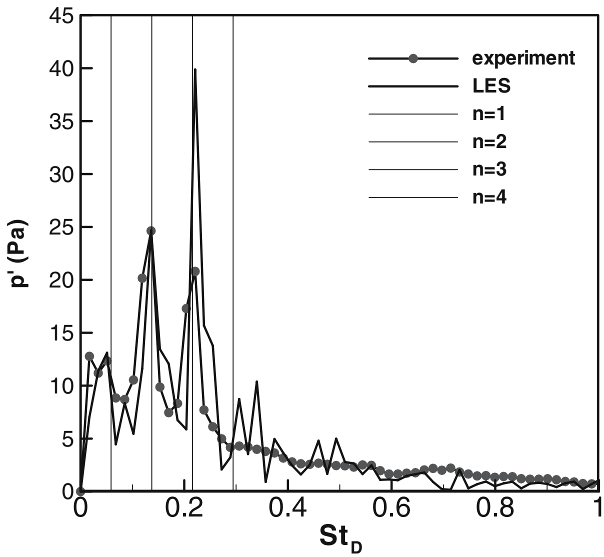

Fig. 7 Spectra of sound pressure at a monitored point on the cavity floor, (x, y, z)=(2.75, 0, 0.625), corresponding to K25 in the experiment

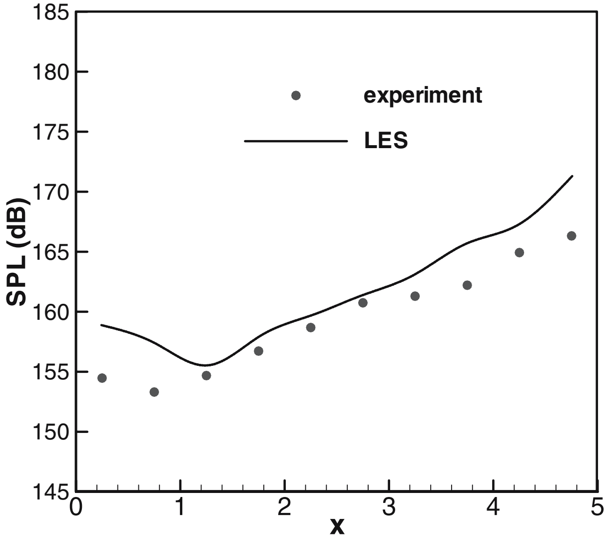

Fig. 8 Comparison of the SPL distributions on the cavity floor along the line of $z=0.625$

3.3 Acoustic analogy for the acoustic far-field of a 3D cavity

In order to apply the hybrid LES-acoustic analogy method to predict sound radiation, the solution procedure in Section 2.3 should be followed. However, several issues need to be addressed.

Firstly, the position of the integration surface is important. Gloerfelt et al. [7] has provided a detailed analysis on this issue for the cavity problem. It is natural to independently consider the contributions from the quadrupole, dipole and monopole sources in Eq. 15. For example, if we use the cavity wall as the integration surface $f=0$, the dipole sources represent the wall reflection, while the monopole sources become zero because of the impermeability. However, the quadrupole sources are not enclosed in the zone $f<0$ in this situation and need to be additionally integrated over a volume. The evaluation of this integration will induce a truncation effect, which causes numerical discrepancies [7]. As the FW-H analogy allows the integration surface or line to be placed in the fluid, Gloerfelt et al. [7] used a line above the cavity and parallel to the floor as the integration line $f=0$ in a 2D cavity case, so that the quadrupole sources are in the zone of $f<0$ and can be omitted in Eq. 15. Gloerfelt et al. [7] also compared three planes at different distances from above the cavity and show that all of them have obtained good agreement with the DNS result, although slight differences exist if all of the quadrupole sources are not included within $f<0$. In our current study using 3D FW-H, we use a plane parallel to the cavity top plate as the integration surface $f=0$. An illustration of the integration surface position, together with the domains for LES and for the observer, is shown in Fig. 9. Early tests showed that similar slight differences in the predicted sound pressure also existed and were observed if the distance between the integration plane and the cavity plate was changed from $s=0.6$ to $s=0.8$. This may be because large vortical structures appear up to $s=0.8$, as observed in Fig. 6. Therefore, the final integration surface is placed at $s=1.0$ to generate the results to be discussed in the following sections.

Other important issues of using the FW-H acoustic analogy concern the selection of integration modes in the frequency domain and the periodicity of sound sources. Because

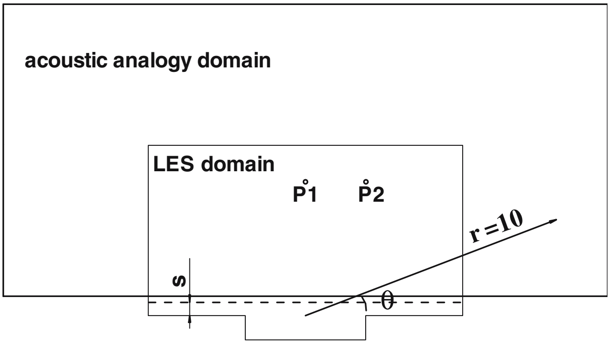

Fig. 9 An illustration of the LES domain and the acoustic analogy domain with an overlapping zone. The *dashed line* indicates the FW-H integration surface f=0. P1 and P2 are two monitoring positions in the acoustic field. r and θ are the distance and angle from the cavity virtual centre, respectively

the integration is in the frequency domain, the integration requires, in theory, that the inputs be strictly periodical. As the cavity sound is generally controlled by the low-frequency tones, a small degree of non-periodicity could induce a relatively large error in the numerical solution. This requirement presents a difficulty in the application of acoustic analogy to the cavity problem. As shown in Fig. 4, the flow does not have strict periodicity, even when it is fully developed. Therefore, the selection of the sampling time period for sound sources is very important. The selection of the integration modes in the frequency domain is also related to the non-periodicity of the cavity flow.

3.3.1 Selection of the sampling period for sound sources

LES results have revealed that, in the low-frequency range, the cavity flow does not have strict periodicity, which is required by the integration modes in the frequency domain. An ad hoc remedy is to check the sound sources and identify a sample period that has an approximate periodicity.

We use the sound source samples at the first instant t=t_1=68.5 as reference values. On the integration surface f=0, the longitudinal flow velocity component at this instant is u_1. For each sample at t_m, we calculate the following norm:

$$E_m = \sum |(u_m - u_1)|, \quad m = 2, \ldots, N \tag{22}$$

where the summation operator Σ is applied to all of the LES grid points on the surface f=0 and N is the total number of samples. Then, we can find an approximate periodicity for the sound sources during the range of $t_1 \le t \le t_M$, which satisfies the following condition:

$$E_M = \min(E_m), \quad m = 2, \ldots, N, \ M \le N \tag{23}$$

With these sound sources, the integration can be carried out using Eq. 15.

Two groups of sound sources are sampled after the flow has established a self-sustained oscillation. Consider the Rossiter modes n=1, 2, and 3. Their Strouhal number values are: St_{D1}=0.0588, St_{D2}=0.137 and St_{D3}=0.216, corresponding to the frequencies of $f_1 = 162$ Hz, $f_2 = 378$ Hz and $f_3 = 595$ Hz, respectively. As shown in Fig. 7, n=2 is one of the main oscillation modes, so the sound monopole Q and dipole F_i sources for the FW-H analogy are recorded for a non-dimensional time period of Δt=Δt_2=1/St_{D2}=7.46, in the interval 68.5≤t≤75.96. The second group of sound sources are sampled during a longer period of $\Delta t \approx 3\Delta t_1 \approx 7\Delta t_2 \approx 11\Delta t_3 = 51$ in the non-dimensional time interval 68.5≤t≤119.5, in an attempt to take into account of all of the three main Rossiter modes n=1, 2 and 3 and to reduce the non-periodicity effects due to sampling. In the first group of sound sources, the sampling period is Δ=0.05828 and 128 samples are taken. In the second group, the sampling period is Δ=0.1 and 512 samples are obtained. The sampling periods correspond to about 230 and 400 times of that of the LES time-marching step. In order to compare with the acoustic analogy, the background pressure has to be subtracted from the LES results:

$$p' = p - p_{\mathrm{av}} \tag{24}$$

where p_{av} is the mean static pressure, averaged during the periods of sampling for the sound sources. For these two groups of sound sources, the p_{av} values are slightly different because of the different sampling times. We use the "sound pressure" defined above to show the wave patterns for the LES results.

In the first group, the only range of sample data for the sound sources that satisfy the periodicity conditions in Eq. 23 is within the interval 68.5≤t≤73.1, with a time period of $\Delta t = 4.6 \approx \Delta t_3$, which corresponds to the third Rossiter mode. The data in the interval 68.5≤t≤75.96, however, does not possess a periodicity corresponding to the second Rossiter mode, as was intended initially. Therefore, when $\Delta t = 4.6 \approx \Delta t_3$ is chosen for sampling the sound sources, Rossiter modes n=1 and 2 are not periodic during the sampling period, which will cause a cut-off error.

Similarly, for the second group of the sampled sound sources, an approximate periodicity exists in the interval 68.5≤t≤117.5, with a time period of Δt=49. This period contains the basic three Rossiter modes n=1, 2 and 3.

3.3.2 Selection of integration modes

Even for the second group of the sampled sound sources, the selected period determined above may not be able to completely satisfy the requirement of strict periodicity. This will introduce a cut-off effect (aliasing error) on the results of the acoustic analogy in the form of high-frequency oscillations. These oscillations are non-physical and should be eliminated.

For the convenience of description, we use the monopole Q as an example and consider a group of N uniformly sampled sound sources:

$$Q_m = Q(t_m), \quad t_m = m\Delta, \ m = 1,\ 2, \ldots,\ N \tag{25}$$

With these N numbers of input, we can obtain N DFT output in the frequency domain:

$$\mathcal{Q}_j = R\left(\mathcal{Q}_j\right) + iI\left(\mathcal{Q}_j\right), \ j = 1,\ \ 2, \ldots, N\,. \tag{26}$$

The frequencies corresponding to $\mathcal{Q}_j$ are [41]:

$$\mathcal{f}_j = \begin{cases} \dfrac{j-1}{N\Delta} & ,\ j = 1, \ldots, \dfrac{N}{2} \\ \pm\dfrac{1}{2\Delta} = \pm\mathcal{f}_c & ,\ j = \dfrac{N}{2}+1 \\ -\dfrac{N+1-j}{N\Delta} & ,\ j = \dfrac{N}{2}+2, \ldots, N \end{cases} \tag{27}$$

In the integration equation of Eq. 15, the Green functions Eqs. 16 and 16a require the dependent variable to be positive. But as seen from Eq. 27, we have $f_1 = 0$, which is the frequency for the direct component of the DFT, Q_1. And if we set $f_{\frac{N}{2}+1} = +f_c$, we have only $N/2$ positive-frequency modes for integration, $f_j \quad (j = 2,\ldots,\frac{N}{2})$; and we can only obtain $\frac{N}{2}$ components of DFT for $p'(\vec{x},\omega_j)$. In order to solve this problem, the physical meaning of the sound pressure has to be considered. That is, because the sound pressure values in the temporal domain, $p(\vec{x},\ t_n)$, are real numbers, their DFT values in the frequency domain must satisfy the following condition:

$$p'(\vec{x},-\omega_j) = \left[p'(\vec{x},\omega_j)\right]^*, \tag{28}$$

where the asterisk denotes the complex conjugation. Making use of Eq. 28, we can obtain N components of DFT for $p'(\vec{x},\omega_j)$ and the sound pressure values at the N instants $p(\vec{x},\ t_m)$, (m=1, 2,..., N), can be obtained through the inversed Fourier transform.

Now we come to the problem of selecting integration modes.

As we mentioned in Fig. 7, the cavity sound is dominated by the discrete tones in the low-frequency range, $0 \le St_D \le 0.5$. The high-frequency components contain very little energy and contribute very little to the sound pressure. In the LES, in principle, it is difficult to discriminate physical and non-physical oscillations in the high-frequency range. Therefore, a cut-off frequency has to be selected to avoid the contamination of non-physical high-frequency modes. On the basis of Fig. 7, the cut-off frequency is chosen to be 0.5, within which, the majority of the source-generating flow oscillations are believed to be captured. For the first group of sound-source samples, the uniform non-dimensional sampling interval is $\Delta = 5.874 \times 10^{-2}$, corresponding to a Nyquist critical frequency of $St_D|_c = \frac{1}{2\Delta} = 8.51$. In the range $0 \le St_D \le St_D|_c$, the positive-frequency modes are j=2,..., 64 (N=128) and they are also uniformly distributed in the frequency domain. Among these, only modes j=2, 3 and 4 are in the range $0 \le St_D \le 0.5$. Similarly, for the second group of sound sources with a sampling interval of Δ=0.1, the modes contributing to the sound generation are j=2, 3,..., 51. When the sample interval is doubled to Δ=0.2 (using one in every two of the sound source samples), the sound-producing modes are j=2, 3,..., 26.

Figures 10 and 11 compare the sound pressures at the two monitoring points shown in Fig. 9, predicted using a subset of sound source samples in the first group. The results show that, during the period of $\Delta t = 4.6 \approx \Delta t_3$, the calculated sound wave patterns using the selected integration modes j=2, 3 and 4 have a reasonable agreement with the LES results, as seen in Fig. 10. The results of the 3D FW-H analogy are better than the 2D results. As expected, by including more integration modes, the predictions of the FW-H acoustic analogy become worse, as judged by the comparison with the LES data, shown in Fig. 11. The appearance of the high-frequency oscillations is attributed to non-physical aliasing errors.

In order to see if improved acoustic predictions can be obtained by a longer sampling time, the second group of sampled sound sources are used for the following results. Figure 12 compares the sound pressures at the monitoring points obtained by LES and by acoustic analogy. The latter uses only one in the every two samples during the period $68.5 \le t \le 117.5$, leading to a total of 256 samples. The selected integration modes are j=2, 3,..., 26, as discussed above. It is seen that, despite small local differences between the LES and the FW-H predictions, the wave patterns including the wave amplitudes and phases of sound pressure oscillations over a long period of time are well predicted by both the 2D and

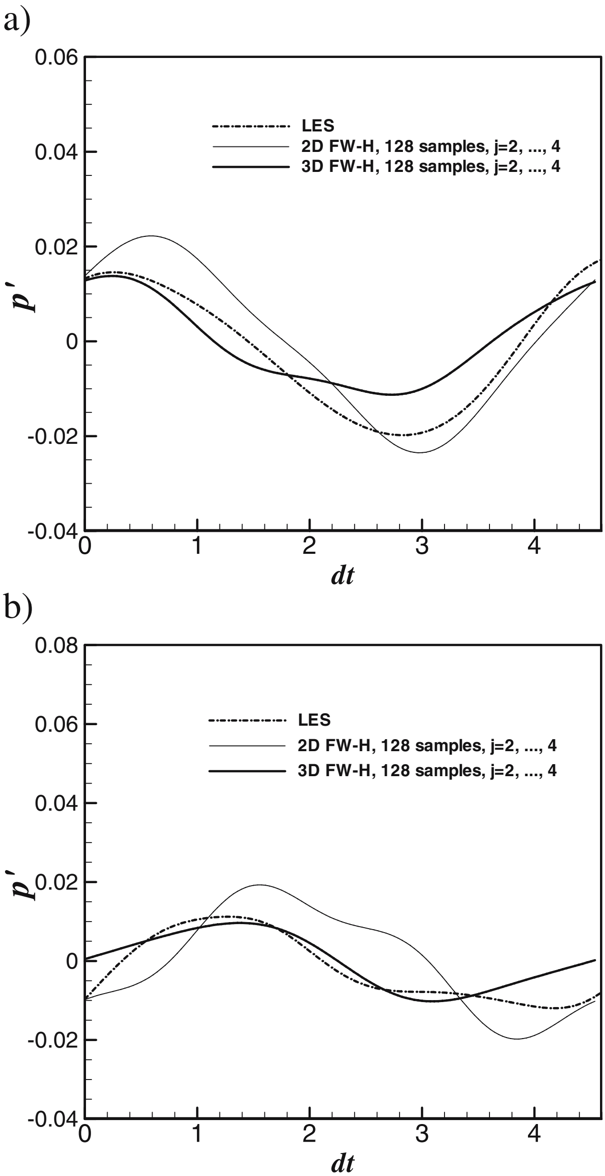

Fig. 10 a, b Comparison of LES and acoustic analogy predictions for the sound pressure histories at monitoring points (**a**) P1 and (**b**) P2. The sound sources are selected from the first group of recordings within $68.5 \leq t \leq 75.96$ with a time period of $\Delta t = 4.6 \approx \Delta t_3$. Only lower modes j=2,..., 4 are selected for the FW-H integration

3D acoustic analogies. For the 2D FW-H, an additional calculation is performed with all of the 512 samples with Δ=0.1, and the predicted profile of the sound pressure duplicates that of the above calculation with 256 samples. This indicates that the sampling interval Δ=0.2 has enough resolution.

Figure 13 compares the sound pressure predictions at the monitored points by LES and by acoustic analogy using more integration modes. Again, high-frequency oscillations appear, which are not seen in the LES. Comparing Figs. 12 with 13, the benefit of selecting appropriate modes for integration becomes clear.

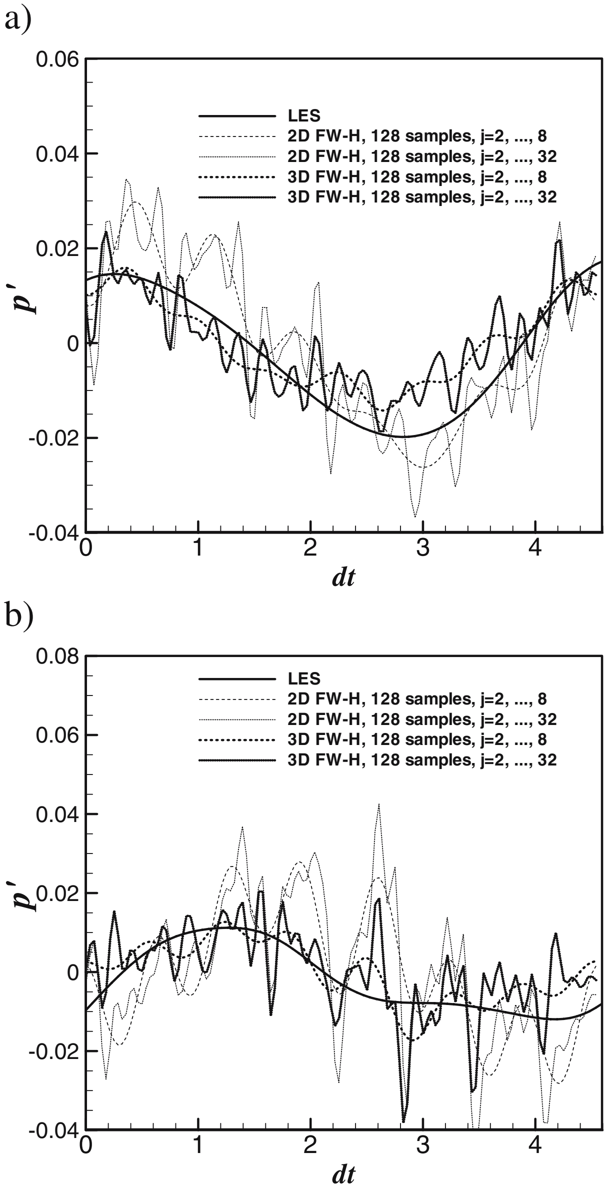

Fig. 11 a, b Comparison of LES and acoustic analogy predictions for the sound pressure histories at monitoring points (**a**) P1 and (**b**) P2. The sound sources are selected from the first group of recordings within $68.5 \le t \le 75.96$ with a time period of $\Delta t = 4.6 \approx \Delta t_3$. Higher modes are included in the FW-H integration

Because the second group of sound sources are in a longer period, therefore, we may be able to have a look at the statistical sound variables in this temporal range. The SPL in the far-field predicted by acoustic analogy discussed in the following is generated using the second group of sound sources.

The SPL distributions in the cavity geometrical central plane are compared in Fig. 14. Note the overlapping zone, in which both LES and acoustic analogy predictions of SPL are available. The directivity of sound radiation in this plane is well predicted by both 2D FW-H and 3D FW-H analogies, with the SPL distribution being predicted slightly better by the 3D FW-H analogy in the overlapped zone.

Fig. 12 a, b Comparison of LES and acoustic analogy predictions for the sound pressure histories at monitoring points (**a**) P1 and (**b**) P2. The sound sources are selected from the second group of recordings within 68.5≤t≤117.5 with a time period of dt=49. Only lower modes are selected for the FW-H integration

a)

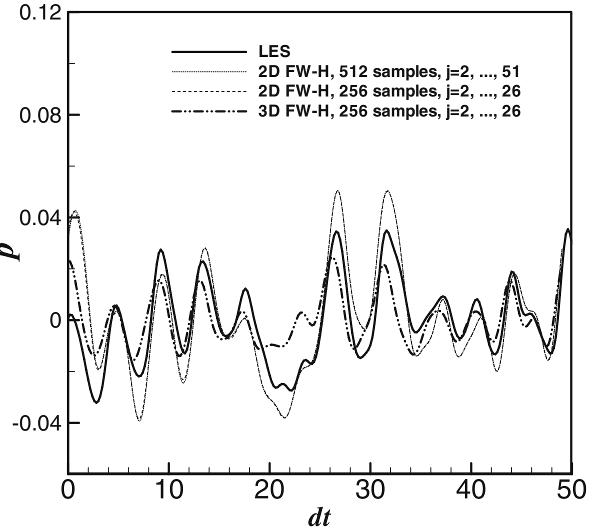

b)

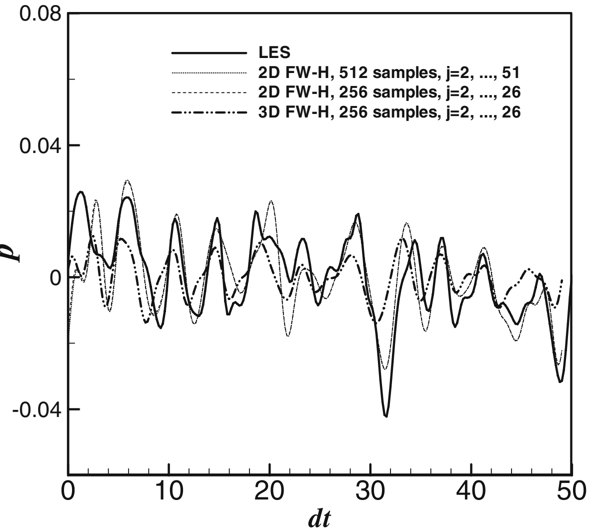

There are some quantitative discrepancies among the LES, the 2D and the 3D FW-H predictions for various reasons, in addition to the unavoidable errors contained in the LES predictions of the near-field sound and the sound sources (which are used for the acoustic analogies). The overlapping zone is a tough place for very accurate comparison, as the very definitions of the sound source and the sound field are not clear-cut, which may explain the differences in the LES and the acoustic analogy predictions. Regarding the quantitative discrepancies between the 2D FW-H and the 3D FW-H analogies, the different propagating behaviours of sound waves in 2D and 3D need to be considered. In the 2D situation, the wave front follows cylindrical spreading and the amplitude of sound decays according to the inverse of square root of the propagation distance [42], i.e. $p' \sim \frac{1}{r^{0.5}}$. In the 3D case,

Fig. 13 a, b Comparison of LES and acoustic analogy predictions for the sound pressure histories at monitoring points (**a**) P1 and (**b**) P2. The sound sources are selected from the second group of recordings within 68.5≤*t*≤117.5 with a time period of d*t*=49. Higher modes are included for the FW-H integration

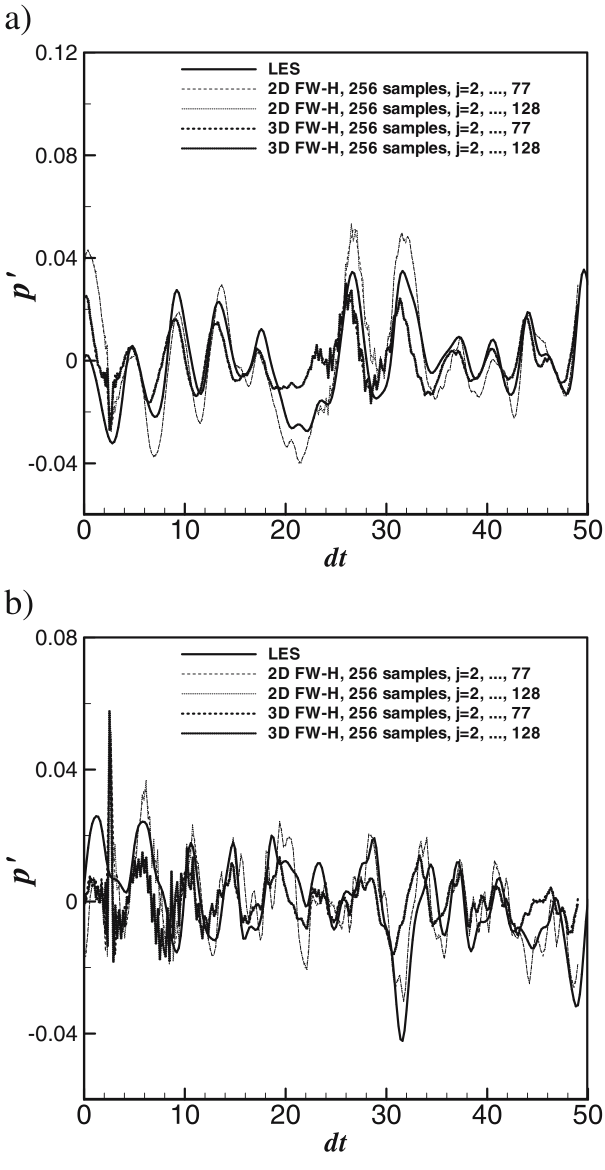

however, the wave front is spherical and the amplitude is $p' \sim \frac{1}{r}$ [33]. That is, the SPL would decay faster with distance in a 3D domain than in a 2D domain. This is qualitatively in agreement with results in Fig. 14, where the SPL predicted by the 3D acoustic analogy is, in general, slightly lower than that predicted by the 2D acoustic analogy. In order to verify the statement, the sound intensity, expressed in terms of the root-mean-square fluctuating pressure p'_{rms}, is calculated by 2D and 3D acoustic analogies along a fixed direction over a longer distance, as shown in Fig. 15. The different rates of decay of 2D and 3D waves are correctly predicted in the present hybrid LES-acoustic analogy approach.

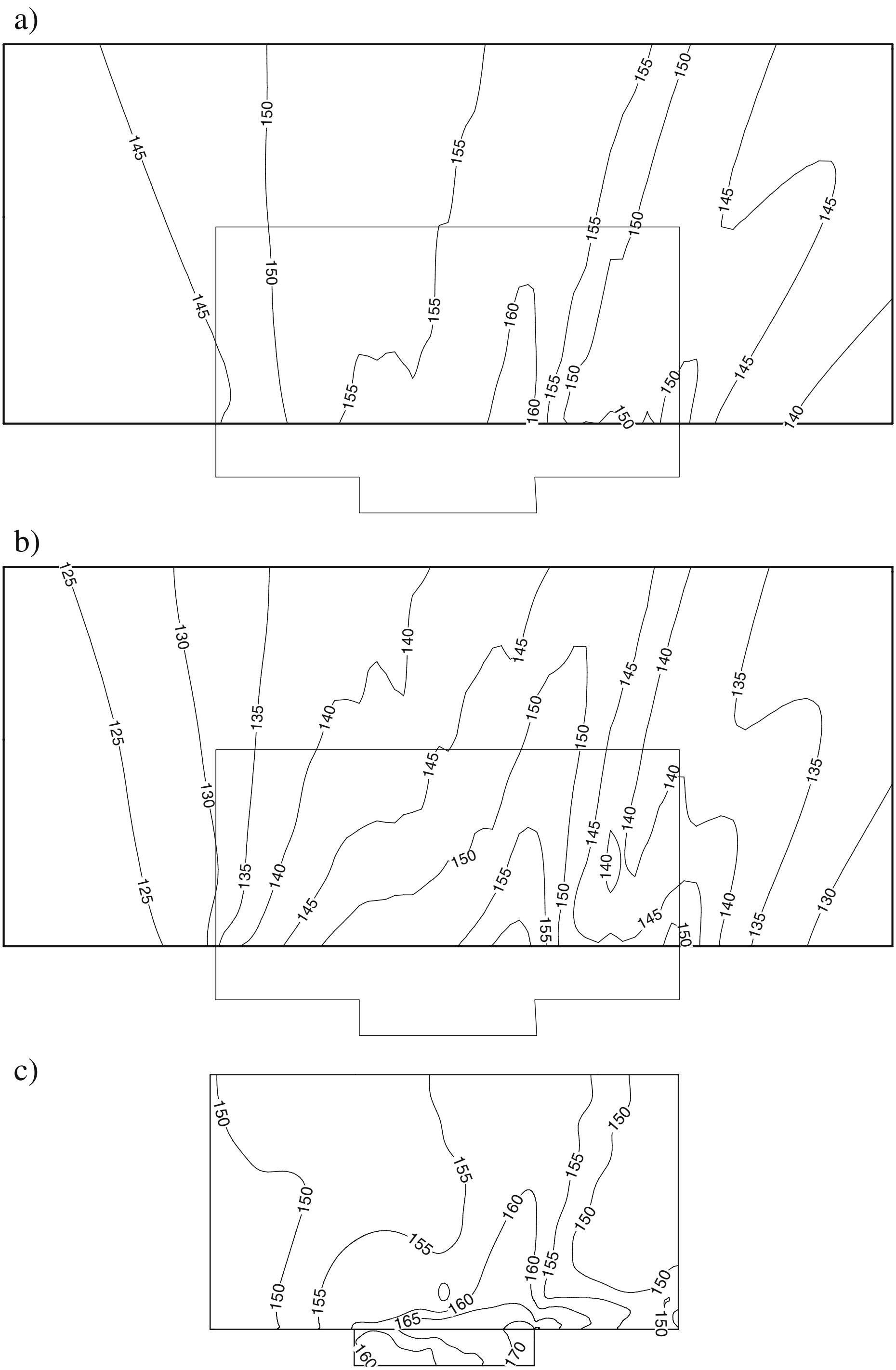

Fig. 14 a–c Comparison of SPL distributions in the cavity central plane predicted by (**a**) 2D FW-H, (**b**) 3D FW-H and (**c**) LES

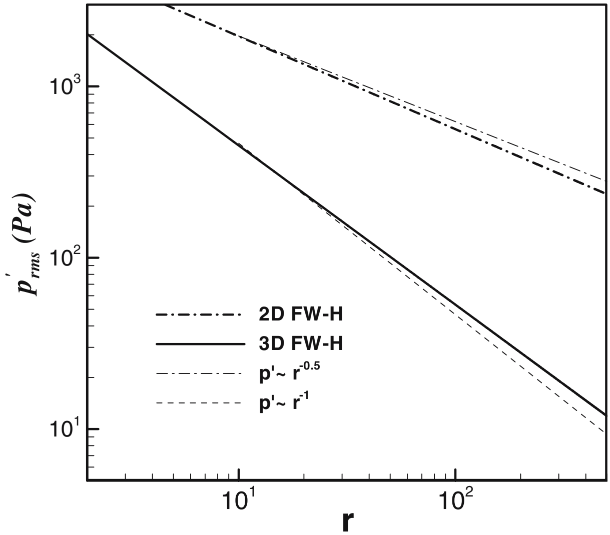

Fig. 15 Decay of sound pressure $p'_{\rm rms}$ in 2D and 3D waves with increasing distance r along the direction θ=75° in the cavity central plane

Finally, a representative 3D distribution of the SPL over a semi-sphere surface centred at the cavity mouth centre and with r=10 is shown in Fig. 16. The colours of the contours indicate the magnitude of the SPL. The peak sound radiation occurs in the cavity central plane over the trailing edge of the cavity, suggesting that the flow impingement on the trailing edge and the rear wall of the cavity is the most significant source of sound.

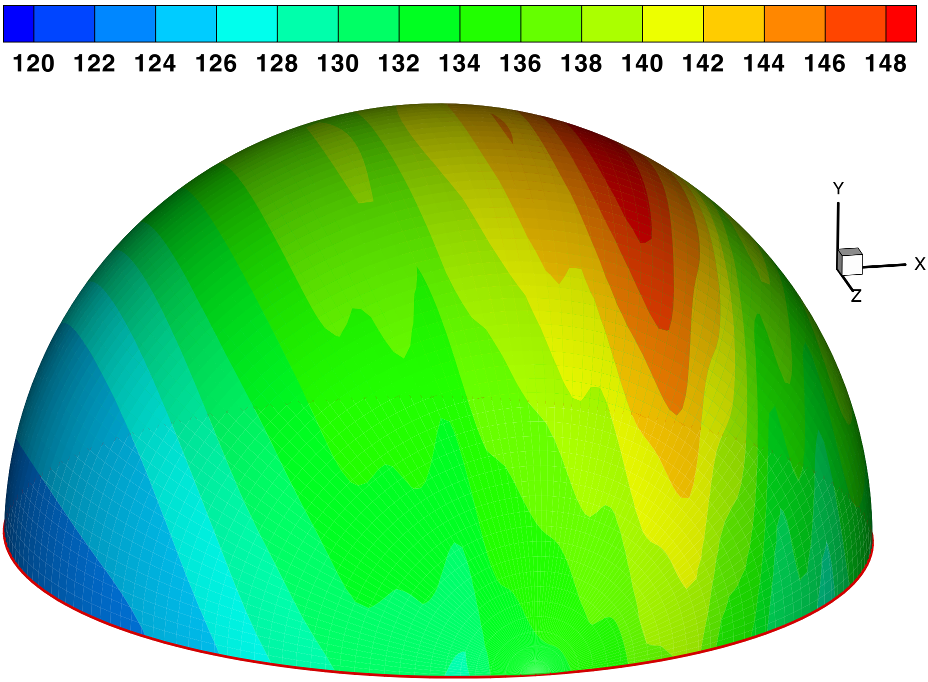

Fig. 16 Three-dimensional FW-H prediction of SPL on the surface of a semi-sphere at r=10 above the cavity, with the cavity central point anchored at (x, y, z)=(2.5, 2.5, 1). The unit of the SPL is dB

4 Summary

A three-dimensional (£D) hybrid large-eddy simulation (LES) acoustic analogy method for computational aeroacoustics(CAA) has been presented for the prediction of open cavity noise. LES is used to compute acoustic sources and the Ffowcs Williams-Hawkings (FW-H) acoustic analogy is employed to calculate the acoustic field. The integration of the FW-H equation is carried out in the frequency domain. As a comparison, the two-dimensional (2D) FW-H analogy is also included. The hybrid method is tested in a realistic 3D cavity flow at a Mach number of 0.85 and a Reynolds number of Re=1.36×106. The LES reveals that the cavity flow has no strict periodicity and that the cavity sound is dominated by the low-frequency tones.

For the successful application of the hybrid approach to cavity aeroacoustics and CAA in general, several technical issues, including the selection of the integration surface and, more importantly, the selection of the integration period and the integration modes, have been discussed in detail. The problems of inappropriate selection in the integration process have been highlighted. The findings suggest that a longer time history of the acoustic sources should be recorded and the periodicity identified before applying the hybrid method. The integration in the frequency domain should include the dominant discrete tones and a suitable range of low-frequency modes, but including higher frequency modes would introduce unphysical fluctuations in the sound pressure level predictions. Finally, 2D and 3D waves propagate differently. When the sound source is strictly 3D, it is important to use a fully 3D acoustic solver, as developed in this study. After these technical issues are solved, the developed hybrid method proves to be reasonably accurate, reliable and computationally cheap as a tool of CAA. Further enhancements may be obtained through: (a) advanced subgrid scale (SGS) models, such as a dynamic model, for fully 3D geometry; (b) adaptive gridding; (c) automatic detection of the boundary of the sound sources; (d) advanced signal processing to detect periodicity and eliminate unphysical modes and so on. Finally, more experimental data are needed in the near- and far-field acoustic fields to further validate the methodology.

Acknowledgements This work was funded by the UK EPSRC and MOD/DSTL under grant no. GR/R85303/01. Thanks are due to Drs. Trevor Birch and Graham Foster at the Defence Science and Technology Laboratory (DSTL), UK, for suppling the experimental data and for their generous support throughout the project. The computing resources were from the UK Turbulence Consortium under EPSRC grant no. EP/D044073/1.

References

1. Takeda, K., Shieh, C.M.: Cavity tones by computational aeroacoustics. Int. J. Comput. Fluid Dyn. **18**(6), 439–454 (2004)
2. Grace, S.M.: An overview of computational aeroacoustic techniques applied to cavity noise prediction. AIAA Paper no. 2001–0510 (2001)
3. Colonius, T.: An overview of simulation, modeling, and active control of flow/acoustic resonance in open cavities. AIAA Paper no. 2001–0076 (2001)
4. Rowley, C.W., Colonius, T., Basu, A.J.: On self-sustained oscillations in two-dimensional compressible flow over rectangular cavities. J. Fluid Mech. **455**, 315–346 (2002)
5. Tam, C.K.W., Webb, J.C.: Dispersion-relation-preserving finite difference schemes for computational acoustic. J. Comput. Phys. **107**(2), 262–281 (1993)
6. Lele, S.K.: Compact finite difference schemes with spectral-like resolution. J. Comput. Phys. **103**(1), 16–42 (1992)

7. Gloerfelt, X., Bailly, C., Juve, D.: Direct computation of the noise radiated by a subsonic cavity flow and application of integral methods. J. Sound Vib. **266**(1), 119–146 (2003)
8. Farassat, F., Myers, M.K.: Extension of Kirchhoff's formula to radiation from moving surfaces. J. Sound Vib. **123**(3), 451–460 (1988)
9. Wang, M., Freund, J.B., Lele, S.K.: Computational prediction of flow-generated sound. Annu. Rev. Fluid Mech. **38**, 483–512 (2006)
10. Zhao, W., Frankel, S., Mongeau, L.: Effects of spatial filtering on sound radiation from a subsonic axisymmetric jet. AIAA J. **38**(11), 2032–2039 (2000)
11. Zhao, W., Frankel, S.H., Mongeau, L.: Large eddy simulations of sound radiation from subsonic turbulent jets. AIAA J. **39**(8), 1469–1477 (2001)
12. Freund, J.B., Lele, S.K., Moin, P.: Numerical simulation of a mach 1.92 turbulent jet and its sound field. AIAA J. **38**(11), 2023–2031 (2000)
13. Bailly, C., Bogey, C.: Contributions of computational aeroacoustics to jet noise research and prediction. Int. J. Comput. Fluid Dyn. **18**(6), 481–491 (2004)
14. Rembold, B., Kleiser, L.: Noise prediction of a rectangular jet using large-eddy simulation. AIAA J. **42** (9), 1823–1831 (2004)
15. Jiang, X., Avital, E.J., Luo, K.H.: Direct computation and aeroacoustic modelling of a subsonic axisymmetric jet. J. Sound Vib. **270**(3), 525–538 (2004)
16. Jiang, X., Avital, E.J., Luo, K.H.: Sound generation by vortex pairing in subsonic axisymmetric jets. AIAA J. **42**(2), 241–248 (2004)
17. Colonius, T., Lele, S.K., Moin, P.: Sound generation in a mixing layer. J. Fluid Mech. **330**, 375–409 (1997)
18. Wang, M., Moin, P.: Computation of trailing-edge flow and noise using large-eddy simulation. AIAA J. **38**(12), 2201–2209 (2000)
19. Zhao, W., Zhang, C., Frankel, S.H., Mongeau, L.: Computational aeroacoustics of phonation, part I: computational methods and sound generation mechanisms. J. Acoust. Soc. Am. **112**(5), 2134–2146 (2002)
20. Nagarajan, S., Lele, S.K.: Sound generation by unsteady airfoil motions: a study using direct computation and acoustic analogy. AIAA Paper no. 2005–2915 (2005)
21. Ffowcs Williams, J.E., Hawkings, D.L.: Sound generation by turbulence and surfaces in arbitrary motion. Philos. Trans. R. Soc., A **264**(1151), 321–342 (1969)
22. Larsson, J., Davidson, L., Olsson, M., Eriksson, L.: Aeroacoustic investigation of an open cavity at low Mach number. AIAA J. **42**(12), 2462–2473 (2004)
23. Ashcroft, G.B., Takeda, K., Zhang, X.: A numerical investigation of noise radiated by a turbulent flow over a cavity. J. Sound Vib. **265**(1), 43–60 (2003)
24. Vreman, B.: Direct and large-eddy simulation of the compressible turbulent mixing layer. Thesis, Universiteit Enschede, The Netherlands (1995)
25. Larchevêque, L., Sagaut, P., Mary, I., Labbé, O.: Large-eddy simulation of a compressible flow past a deep cavity. Phys. Fluids **15**(1), 193–210 (2003)
26. Sandham, N.D., Yao, Y.F., Lawal, A.A.: Large-eddy simulation of transonic turbulent flow over a bump. Int. J. Heat Fluid Flow **24**(4), 584–595 (2003)
27. Sandham, N.D., Li, Q., Yee, H.C.: Entropy splitting for high-order numerical simulation of compressible turbulence. J. Comput. Phys. **178**(2), 307–322 (2002)
28. Yee, H.C., Sandham, N.D., Djomehri, M.J.: Low-dissipative high-order shock-capturing methods using characteristic-based filters. J. Comput. Phys. **150**(1), 199–238 (1999)
29. Carpenter, M.H., Nordstroem, J., Gottlieb, D.: A stable and conservative interface treatment of arbitrary spatial accuracy. J. Comput. Phys. **148**(2), 341–365 (1999)
30. Lighthill, M.J.: On sound generated aerodynamically: I. General theory. Proc. R. Soc. Lond. A **211** (1107), 564–587 (1952)
31. Curle, N.: The influence of solid boundaries upon aerodynamic sound. Proc. R. Soc. Lond. **A231**(1187), 505–514 (1955)
32. Lockard, D.P.: An efficient, two-dimensional implementation of the Ffowcs Williams and Hawkings equation. J. Sound Vib. **229**(4), 897–911 (2000)
33. Howe, M.S.: Acoustics of fluid–structure interaction. Cambridge University Press, Cambridge, UK (1998)
34. Dowling, A.P., Ffowcs Williams, J.E.: Sound and sources of sound, Chapter 9, pp. 207–208. Horwood Publishing, Westergate, UK (1983)
35. De, M.J., Henshaw, C.: M219 cavity case. In: Verification and validation data for computational unsteady aerodynamics. Technical Report RTO-TR-26, AC/323(AVT)TP/19, 453–472 (2000)
36. Larchevêque, L., Sagaut, P., Le, T.-H., Comte, P.: Large-eddy simulation of a compressible flow in a three-dimensional open cavity at high Reynolds number. J. Fluid Mech. **516**, 265–301 (2004)

37. Thompson, K.W.: Time-dependent boundary conditions for hyperbolic systems, II. J. Comput. Phys. **89** (2), 439–461 (1990)
38. Hunt, J.C.R., Wray, A.A., Moin, P.: Eddies, streams, and convergence zones in turbulent flows. In: Proceedings of the 1988 Summer Program (Center for Turbulence Research, Stanford, CA), pp. 193–208 (1988)
39. Bogey, C., Bailly, C.: LES of a high Reynolds, high subsonic jet: effects of the subgrid modellings on flow and noise. AIAA Paper no. 2003–3557 (2003)
40. Gloerfelt, X.: Large-eddy simulation of a high Reynolds number flow over a cavity including radiated noise. AIAA Paper no. 2004–2863 (2004)
41. Press, W.H., Teukolsky, S.A., Vetterling, W.T., Flannery, B.P.: Numerical recipes in FORTRAN, 2nd edn. Cambridge University Press, Cambridge, UK (1992)
42. Guo, Y.P.: Application of the Fjowcs Williams/Hawkings equation to two-dimensional problems. J. Fluid Mech **403**, 201–221 (2000)